33RD CONGRESS
OF THE INTERNATIONAL COUNCIL
OF THE AERONAUTICAL SCIENCES
STOCKHOLM, SWEDEN, 4-9 SEPTEMBER, 2022

ICAS 2022 SWEDEN

PREDICTING STEADY LIFT AND DRAG COEFFICIENT OF TANDEM AIRCRAFT USING PRANDTL'S EXTENDED LIFTING-LINE THEORY IMPLEMENTED UNDER ASWING

R.JAN[1], J-M Moschetta[2] & J-P Condomines[3]

[1]ISAE Supaero/DAEP: Toulouse, 31400, France
[2]ISAE Supaero/DAEP: Toulouse, 31400, France
[3]ENAC: Toulouse, 31400, France

Abstract

The Steady form of ASWING's extended non-linear LLT is recalled and benchmarked using both experimental and CFD data. A tandem configuration is used as a strong vortices interaction example with a low aspect ratio to present the benefit of such software to predict lift and drag coefficients of multiple lifting surfaces. Secondly, the model is also benchmarked for an elliptical wing with a modified XFOIL analysis to improve drag prediction of a chord varying planform. Finally, ASWING is used as a performance prediction tool in a parametric study to maximize the CL/CD ratio of a tandem aircraft with an elliptical planform and taking into account the effect of the fuselage on lift and drag.

Keywords: Modern lifting line theory, pre-stall, tandem aircraft,steady wake interaction

List of Symbols

C_L, c_l	3D and 2D lift coefficient
C_D, c_d	3D and 2D drag coefficient
α	angle of attack
β	side slip angle
$\vec{V}$	relative airflow velocity
$\vec{V_\infty}$	freestream velocity
$\vec{V_{ind}}$	induced velocity
$\vec{V_{gust}}$	gust velocity
$\vec{V}_\perp$	local orthogonal velocity
Γ	circulation variable
Ω	rigid rotation rate vector

List of Acronyms

CL	Lift Coefficient
CD	Drag Coefficient
CFD	Computational Fluid Dynamic
LLT	Lifting Line Theory
ASWING	software name
PG	Plandtl-Glauert
csn	local airfoil frame, c is aligned with the zero lift line, s in the spanwize direction

1. Introduction

Since the past decade, Unmanned Aerial Vehicles (UAV) are widely used for different applications (military or civilian). Different types of layouts exist regarding UAVs to answer to many different types of missions. One among them is known as tandem aircraft or multiple lifting surface devices. Those have been studied in the early 80s [1], [2] and are still of interest for their different advantages recall by the literature.

Regarding the advantages, tandem aircraft are known to be more efficient in induced drag reduction than the traditional layout. Wingspan can be reduced with the same stiffness inducing better lateral flight stability. Tandem UAVs are also extremely compact, with folded wings [3], [4]. Moreover, they perform maximum CL/CD on a wider angle of attack range leading to a more efficient flight envelope [5]. Finally, tandem aircraft performs maximum CL/CD ratio to higher CL than for the single wing layout leading to the use of a smaller wetted area.

Among the drawbacks, one can recall that usually a shorter chord is used on tandem aircraft leading to a lower Reynolds number, increasing the airfoil viscous and pressure drag. However, choosing an adapted one(with low Re number) can damp those effects. [5] have also witnessed that the winglet efficiency decrease with dual-wing configuration. Research works are still ongoing regarding the design of adapted winglets to Tandem configuration which is out of this article's scope.

According to the advantages of the Tandem configuration, many parametric studies have been full-filled in the past 30 years on different low and high fidelity numerical models and with sometimes some experimental correlations [1], [3], [5], [6], [7], [8],[9]. However those has been usually done for low to moderated angles of attack. Moreover, the viscous drag and fuselage effects are usually omitted and pre-stall and post-stall behaviour hasn't been studied. This article aims at recalling a low fidelity extended model of the non-linear lifting theory embedded in ASWING. The needed theoretical background is recalled and benchmarked with both CFD and experimental data from the literature, to highlight the capability of ASWING to predict lift and drag of tandem aircraft from low to post-stall angle of attack. Finally, a multiple parameter study is presented to converge from a baseline geometry to a pre-design optimal one.

2. Extended Non linear lifting line theory for multiple lifting surface configuration

2.1 Aerodynamic loads:

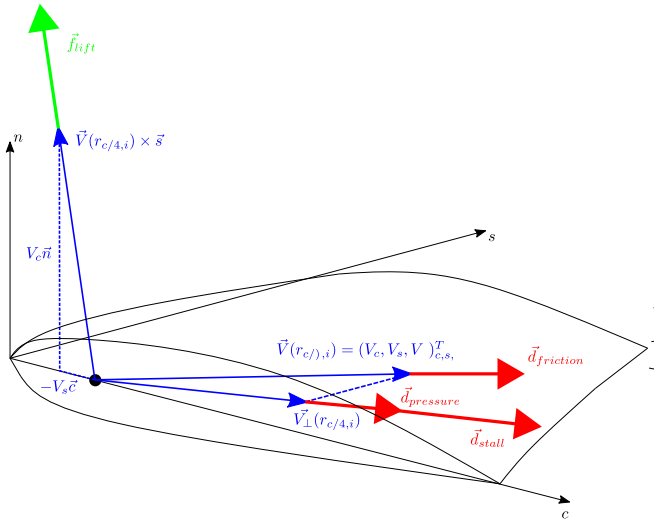

Figure 1 – Wing : Lift and drag contributions in the local csn frame

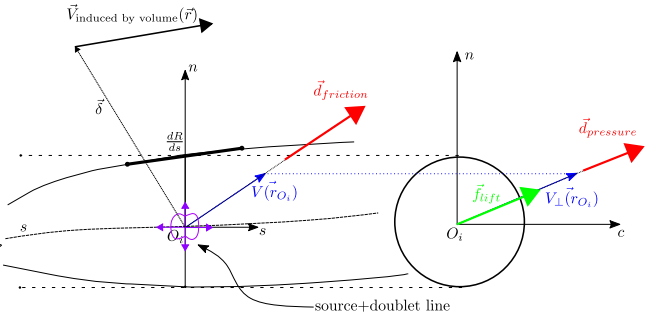

Figure 2 – Fuselage : Lift, drag contributions and volume influence on local velocity

In ASWING ([10] [11]), the lift generated by a surface beam is given by the unsteady form of Kutta Jukowski theorem, however here, one will only recall the steady part [10] of it in equation (1). $\vec{V}$ denotes the local net stream velocity evaluated at vortex's horseshoes boundary position $\vec{r_{h,v}}$.

$$\vec{f}_{\text{lift}} = \rho\Gamma\vec{V} \times \hat{s} \tag{1}$$

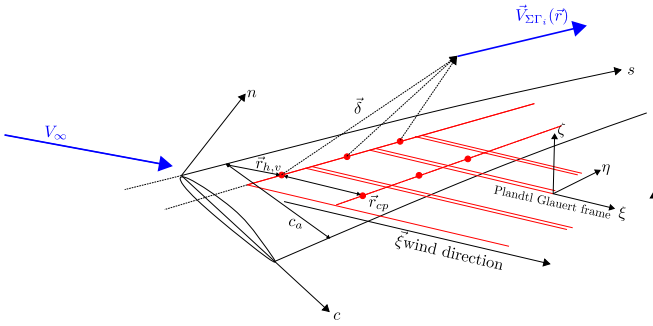

Figure 3 – Induced velocity from bound vortices and circulation mode represented by wind aligned trailing vorticities

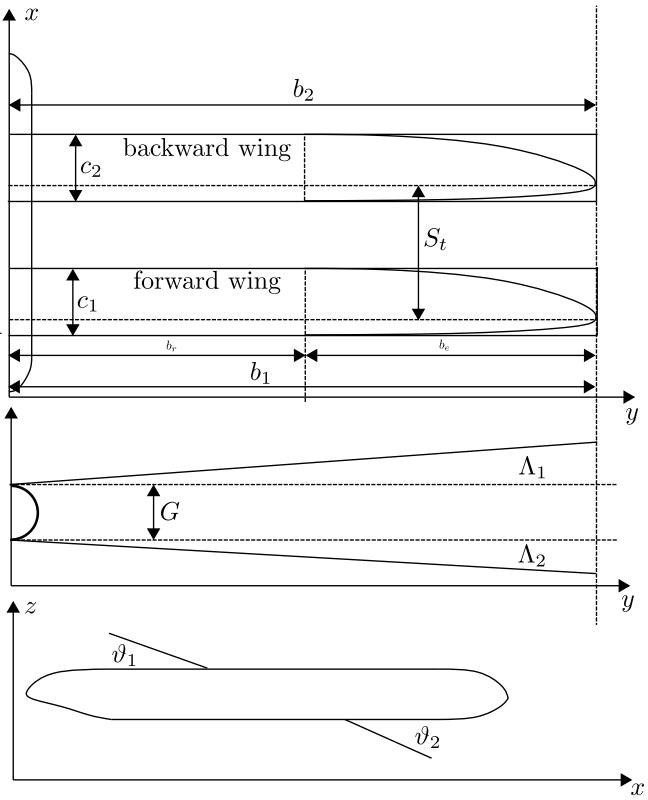

Figure 4 – Tandem aircraft : geometrical parameters

where Γ is the circulation given by :

$$\Gamma(s) = \sum_{k=1}^{K} A_k \sin\left(k \arccos\left(\frac{s}{s_{\max}}\right)\right) \tag{2}$$

For the next sections, $\vec{V}$ must be considered as the local stream velocity and its expression is given by

$$\vec{V}(\vec{r}) = \vec{V}_\infty - \vec{\Omega} \times \vec{r} + \vec{V}_{\text{ind}}(\vec{r}) + \vec{V}_{\text{gust}}(\vec{r}) - \vec{v}(\vec{r}) \tag{3}$$

where $\vec{V}_{\text{ind}}$ embeds the velocity influence of vortices, beam volume and engine jets. In the case of that paper, some terms in (3) vanish like the first one because one will present results for an anchored aircraft (restricted static movement). Moreover, the last term vanishes as well because it accounts for the unsteady effect of the local beam nodes deflection. Finally, no gust will be considered in that study so (3) becomes:

$$\vec{V}(\vec{r}) = \vec{V}_\infty + \vec{V}_{\text{ind}}(\vec{r}) \tag{4}$$

with $\vec{V}_{\text{ind}}$ defined as

$$\vec{V}_{\text{ind}}(\vec{r}) = \sum_{k=1}^{K} \vec{v}_k(\vec{r}) A_k + \vec{w}_{\text{vol}}(\vec{r}) V_\infty \tag{5}$$

In the next section, $\vec{V}$ will be evaluated at different $\vec{r}$ positions but remains defined by the same expression.
Note that the cross product $\vec{V} \times \hat{s}$ imposes the lift to lay in the local cn plane as shown in figure 1
The lift generated by a fuselage beam is given by the steady form of the slender body theory:

$$\begin{aligned} \vec{f}_{\text{lift}} &= \rho \vec{V}_\perp (\vec{V} \cdot \hat{s}) 2\pi R \frac{dR}{ds} \\ \vec{V}_\perp &= \vec{V} - (\vec{V} \cdot \hat{s})\hat{s} \end{aligned} \tag{6}$$

where $\vec{V}_\perp$ is the local stream velocity component in the cn plane. $\vec{V}_\perp$imposes the direction of the lift force as described in figure 2. In the case of a fuselage beam, the velocities vector is evaluated at the centre of the cross-section at position $\vec{r_{O_i}}$ where i denotes the beam nodes index. Note that if the cross-section does not vary over the beam arc, the fuselage beam won't generate any lift.
Regarding the drag forces, one must denote as-well surface and fuselage beams. The surface beam drag is expressed by equation (7) and is composed of 3 terms. A friction drag component, a pressure drag and a post-stall contribution. The direction of those forces are imposed by the local normal and net velocities evaluated at horseshoe vortex boundaries positions $\vec{r}_{h,v}$ as depicted in figure 1. cd_f and cdp can be obtained thanks to XFOIL software [12] by interpolating the data in the linear range of angle of attack. The post-stall contribution will be treated in the later related section.

$$\begin{aligned} \vec{f}_{\text{drag}} &= \frac{1}{2}\rho|\vec{V}|\vec{V}\bar{c}c_{d_f} + \frac{1}{2}\rho\left|\vec{V}_\perp\right|\vec{V}_\perp\bar{c}c_{d_p} + 2\rho\frac{\vec{V}_\perp}{\left|\vec{V}_\perp\right|}(\vec{V}\cdot\hat{n})^2_{c.p.}\bar{c} \\ \vec{f}_{\text{drag}} &= \vec{d}_{friction} + \vec{d}_{pressure} + \vec{d}_{poststall} \end{aligned} \tag{7}$$

For fuselage beams, there are only friction and pressure contribution denoted by the equation (8) cdf and cdp are the skin friction and the drag coefficient of a cylinder.

$$\begin{aligned} \vec{f}_{\text{drag}} &= \frac{1}{2}\rho|\vec{V}|\vec{V}2Rc_{d_f} + \frac{1}{2}\rho\left|\vec{V}_\perp\right|\vec{V}_\perp 2Rc_{d_p} \\ &= \vec{d}_{friction} + \vec{d}_{pressure} \end{aligned} \tag{8}$$

The pressure and skin friction are described in figure 2 c_{d_f} and c_{d_p} are the skin friction and the drag coefficient of a cylinder. c_{d_p} varies from 1.4 to 0.2 depending on the Reynold number but for UAV applications, one would assume 1.2. Regarding the skin friction drag, one can use the 2 empirical Blasius formulas recalled by (9). Depending on where the propeller is placed on the geometry, one would advise the turbulent formula for propeller placed near or on fuselage beam.

$$\begin{aligned} C_{f-\text{ laminar}} &= \frac{1.328}{\sqrt{Re_l}} \\ C_{f-\text{ turbulent}} &= \frac{0.427}{[\log Re_l - 0.407]^{2.64}} \end{aligned} \tag{9}$$

Regarding aerodynamic forces, one won't go further because the paper does not aim at providing a stability analysis. The reader must have in mind, that ASWING's model computes the local aerodynamic momentum contributions of the lift, drag and 2D cm profile.

2.2 Prandtl-Glauert Transformation for compressibility effect:

In order to compute aerodynamic loads, one must solve the discrete lifting line theory. However one solves it in the Prandtl-Glauert space to account for the compressibility effect. Consequently, the trailing edges of the horseshoes' legs are wind aligned as described in figure 3. The Prandtl-Glauert axis given by equation (10)

$$\begin{Bmatrix} \xi \\ \eta \\ \zeta \end{Bmatrix} = \begin{bmatrix} \bar{P} \end{bmatrix} \begin{Bmatrix} x \\ y \\ z \end{Bmatrix} \tag{10}$$

$$\bar{P} = \begin{bmatrix} \cdots & \vec{\xi}^T & \cdots \\ \cdots & \hat{\eta}^T & \cdots \\ \cdots & \hat{\zeta}^T & \cdots \end{bmatrix} = \begin{bmatrix} \frac{1}{\lambda}\cos\alpha\cos\beta & -\frac{1}{\lambda}\sin\beta & \frac{1}{\lambda}\sin\alpha\cos\beta \\ \cos\alpha\sin\beta & \cos\beta & \sin\alpha\sin\beta \\ -\sin\alpha & 0 & \cos\alpha \end{bmatrix}_{\text{wind}} \tag{11}$$

where $\lambda = \sqrt{1-M^2_{\text{PG}}}$ is the stretching scalar. The Prandtl-Glauert Mach number is actually the real infinite Mach number. Finally $\vec{\xi}$ is aligned with the wind direction as illustrated by figure 3 and equation (12)

$$\vec{\xi} = \frac{1}{\sqrt{1-M^2_{\text{PG}}}} \begin{Bmatrix} \cos\alpha\cos\beta \\ -\sin\beta \\ \sin\alpha\cos\beta \end{Bmatrix}_{\text{wind}} \tag{12}$$

Proceeding to this transformation recovers a compressible flow problem in the transform state space which can be integrated to get the influence velocities function of vortices and volumes.The equation (13) states the transform problem.

$$\begin{gathered}(1-M_{\mathrm{PG}}^2)\frac{\partial^2\phi}{\partial x^2}+\frac{\partial^2\phi}{\partial y^2}+\frac{\partial^2\phi}{\partial z^2}=0\\ \downarrow\\ \frac{\partial^2\phi}{\partial \xi^2}+\frac{\partial^2\phi}{\partial \eta^2}+\frac{\partial^2\phi}{\partial \zeta^2}=0\end{gathered} \tag{13}$$

The velocities in the cartesian space are then obtained ("stretched back") with transposal P matrix.

$$\begin{aligned}\left\{\begin{array}{c}\partial\phi/\partial x\\ \partial\phi/\partial y\\ \partial\phi/\partial z\end{array}\right\}&=\left[\begin{array}{ccc}\xi_x & \eta_x & \zeta_x\\ \xi_y & \eta_y & \zeta_y\\ \xi_z & \eta_z & \zeta_z\end{array}\right]\left\{\begin{array}{c}\partial\phi/\partial\xi\\ \partial\phi/\partial\eta\\ \partial\phi/\partial\zeta\end{array}\right\}\\ &=\left[\begin{array}{c}\bar{P}^T\end{array}\right]\left\{\begin{array}{c}\partial\phi/\partial\xi\\ \partial\phi/\partial\eta\\ \partial\phi/\partial\zeta\end{array}\right\}\end{aligned} \tag{14}$$

Note that the stretching factor λ tends to zero with Mach number reaches 1. This transformation thus diverges in the surrounding of transonic flow. It will however recover correctly the compressibility effect of flow up to $M_\infty = 0.7$

2.3 Vortex influence function:

Circulations modes are solved by integrating the Biot Savart law over the circulation of **all** beams. The discrete bound are placed at a quarter chord in each local cn plane and the trailing legs are aligned with the wind direction. The modal contribution of each circulation mode is given by (15)

$$\begin{aligned}\Gamma_k &= A_k \sin\left(k\arccos\left(\frac{s_a}{s_{max}}\right)\right)\\ \text{where}\quad \theta_a &= \frac{1}{2}(\theta_i+\theta_{i+1})\end{aligned} \tag{15}$$

where θ_a is an averaged mid point and the averaged interpolated position is given by:

$$\vec{r}_a = \vec{r}_i + (\vec{r}_{i+1}-\vec{r}_i)\frac{s_a-s_i}{\Delta s} \tag{16}$$

As mentioned earlier, the position of the horseshoe bound vortices is downstream from a quarter chord in the wind direction as shown on figure 3

$$\vec{r}_{h.v.} = \vec{r}_a + \frac{\bar{c}/4-\bar{x}_o}{|\vec{\xi}\times\hat{s}|}\vec{\xi} \tag{17}$$

And the control points are as-well downstream from approximately half a chord distance in the wind direction

$$\vec{r}_{c.p.} = \vec{r}_{h\cdot v.} + \frac{h\bar{c}_a}{|\vec{\xi}\times\hat{s}|}\vec{\xi} \tag{18}$$

where h is defined by:

$$h = \frac{1}{4\pi}\frac{dc_\ell}{d\alpha} \tag{19}$$

with $\frac{dc_\ell}{d\alpha}$ is the 2D local slope of the airfoil.

The velocity induced by vortices are then obtained by integrating the Biot-Savart law in the Prandtl-Glauert space to account for compressibility effect and bring back to the physical space using the transformation matrix:

$$\begin{aligned}\vec{v}_k(\vec{r}) &= \left[\ \bar{P}\ \right] \left\{ \begin{array}{c} \partial\phi/\partial\xi \\ \partial\phi/\partial\eta \\ \partial\phi/\partial\zeta \end{array} \right\}_k (\vec{r}) \\ &= \left[\ \bar{P}^T\ \right] \left\{ \frac{1}{4\pi} \sum_{i=1}^{I-1} \sin(k\theta_a) \int \frac{d\vec{\ell} \times \vec{\delta}}{\delta^3} \right\}\end{aligned} \tag{20}$$

with:

$$d\vec{\ell} = d\vec{r}_P = \bar{\bar{P}} d\vec{r}$$

where $\vec{\delta}(\vec{r})$ is the relative vector between the position where the induced velocity must be evaluated and the position of a small element on the bound or trailing horseshoe.

$$\vec{\delta} = \vec{r}_P - \vec{r}_P(\ell) = \bar{\bar{P}} \left\{ \vec{r} - \vec{r}_{(\ell)} \right\}$$

$$\vec{v}_k = \left[\bar{P}^T\right] \left\{ \frac{1}{4\pi} \sum_{i=1}^{I-1} \sin(k\theta_a) \int \frac{d\vec{\ell} \times \vec{\delta}}{(\delta^2 + \varepsilon^2)^{3/2}} \right\} \tag{21}$$

Note that aligning the trailing vortices with the freestream direction gives better accuracy for high angle of attack and sideslip because the vortices are shed by the airflow and are no more aligned with the local csn frame.

2.4 Volume influence function:

Using source/length and doublet/length defined by equations (22), one can recover the volume contribution to induced velocity. Indeed they impose the flow tangency on the circular beam of cross sectional radius R. Densities are given in the Prandtl-Glauert frame to take into account compressibility effects.

$$\begin{aligned}\sigma(\ell) &= \frac{d\left(\pi R^2\right)}{d\ell} (\vec{\xi} \cdot \hat{\ell}) \\ \vec{v}(\ell) &= 2\pi R^2 (\vec{\xi} - (\vec{\xi} \cdot \hat{\ell}) \hat{\ell})\end{aligned} \tag{22}$$

The induced velocity is then given by the integrated Biot Savart law for both densities and given by equation (23)

$$\vec{w}_{\text{vol}}(\vec{r}) = \left[\bar{P}^T\right] \left\{ \frac{1}{4\pi} \int \left[\frac{\sigma\vec{\delta}}{(\delta^2 + \varepsilon^2)^{3/2}}\ left. + \frac{\vec{v}\delta^2 - 3(\vec{v} \cdot \vec{\delta})\vec{\delta}}{(\delta^2 + \varepsilon^2)^{5/2}} \right] d\ell \right\} \tag{23}$$

where δ is the relative vector between $\vec{r}$ (where $\vec{w}_{\text{vol}}$is evaluated) and $\vec{r}(l)$ the position of each densities. δ is expressed in the Prandtl-Glauet frame, because the overall integration is done in that space as mentionned earlier. Equations (23) and (22) can be used to recover the thickness effect of a wing, by setting the local radius as half of the maximum airfoil thickness. Volumic effects are mostly evaluated for the fuselage which is usually wider than wings.

2.5 Separation and Stall modeling:

Stall and separation are modelled based on finite swept-wing theory. It results in a non zero normal velocity in the Kutta flow tangency condition described by

$$\vec{V}(\vec{r}_{c.p.}) \cdot \hat{n}_{c.p.} - \frac{V_\perp}{4\pi h} K_s f_{\text{stall}}(c_\ell) = 0 \tag{24}$$

where f_{stall} is a post stall function :

$$f_{\text{stall}} = \Delta c_\ell \log \frac{1+\exp\left[\left(c_\ell - c_{\ell_{\max}}\right)/\Delta c_\ell\right]}{1+\exp\left[\left(c_{\ell_{\min}} - c_\ell\right)/\Delta c_\ell\right]} \tag{25}$$

This function aims at modifying the 2D lift slope as followed

$$\frac{dc_\ell}{d\alpha} \simeq \begin{cases} 4\pi h, c_{\ell\min} < c_\ell < c_{\ell_{\max}} \\ 4\pi h/\left(1+K_{\text{s}}\right), c_\ell < c_{\ell\min}, c_{\ell\max} < c_\ell \end{cases} \tag{26}$$

At the light of the separation, the non respected flow tangency condition implies a pressure profile additional drag

$$c_d = 4\left(\frac{\vec{V}\cdot\hat{n}}{V}\right)^2 \simeq 4\left(\frac{K_{\text{s}}}{1+K_{\text{s}}}\right)^2\left(\sin\alpha - \frac{c_{\ell\max}}{4\pi h}\right)^2, c_\ell > c_{\ell_{\max}} \tag{27}$$

The reader must acknowledge that cl won't fall back after stall but reach an asymptote, which is not accurate with physical behaviour. However, it is very useful for modeling for a near and early stall. The user does not recommend the study for an extreme angle of attack because it wont recover the histeresis effect of post stall

2.6 Circulation coefficient constraints

Denoting K the number of circulation modes of all the lifting surfaces, one must provide K constraints equations to solves the overall problem. Those are imposed by the modified Kutta condition of flow tangency on the surface at each discrete control point given by equation (28)

$$\vec{V}\left(\vec{r}_{c.p.}\right)\cdot\hat{n}_{c.p.} - \frac{V_\perp}{4\pi h}K_{\text{s}}f_{\text{stall}}\left(c_\ell\right) = 0 \tag{28}$$

The quasi normal vector $\hat{n}_{c.p.}$ is defined by

$$\hat{n}_{cp.} = \bar{T}^T\begin{Bmatrix}\sin\alpha_A \\ 0 \\ \cos\alpha_A\end{Bmatrix} \tag{29}$$

where α_A embed the effect of flaps local twist and zero lift angle of attack:

$$\alpha_A = \alpha_{Ao} + \frac{dc_\ell/d\delta_{p_1}}{dc_\ell/d\alpha}\delta_{p_1} + \frac{dc_\ell/d\delta_{p_2}}{dc_\ell/d\alpha}\delta_{Y_2}\ldots \tag{30}$$

Note that the second term accounts reasonably for separation and stall. A more detailed expression of (28) gives :

$$\sum_{i=1}^{I-1}\left(\vec{V}\left(\vec{r}_{c.p.}\right)\cdot\hat{n}_{c.p.}\right)_a \sin\left(k\theta_a\right)\Delta\theta - \frac{V_\perp}{4\pi h}K_{\text{s}}f_{\text{stall}}\left(c_\ell\right) = 0 \quad k\in[1\ldots K] \tag{31}$$

Recalling $\vec{V}\left(\vec{r}_{c.p.}\right)$ expressions (3) and (5), it includes the vortex influence functions that contains the ciculation modes. Consequently one gets K well constrained equations allowing the solution of the overall problem.

3. Experimental and CFD comparison with ASWING's LLT

Lift and Drag coefficient prediction of ASWING' steady LLT must be compared with experimental and CFD data. Moreover one must seek the most interactive case to ensure that the presented theoretical results predict correctly lift and drag even in the worst case. Consequently, the tandem configuration is very appropriate because there is a lot of interaction and impact between each wing and their respected generated vortices. [1] provides a set of data for four different tandem wings configuration. The tandem configuration is described by figure 4. The experimental campaign has been run in a 2 by 3 meters low Reynolds, closed throat wind tunnel. Unfortunately, the report only provides one set of corrected data. However, it is the worst case as it is the one for positive gap and minimum stagger

	Tandem aircraft 1[1]	Tandem aircraft 2 [3]
Airfoil	NASA-GAW2	NACA4309
Speed	V = 69.15m/s	V = 30m/s
Re	1.4E6	2.65E5
Planform	Rectangular	Rectangular
c_{canard}	0.22m	0.129m
c_{wing}	0.305m	0.129m
b_{wing}	1.83m	2.0425m
b_{canard}	1.29m	2.1805m
ϑ_{canard}	2	0
ϑ_{wing}	0	0
G (gap)	$+0.5c_{wing}$	-0.101m
S (Stagger)	$1.63c_wing$	0.89m
S_{ref}	$0.56m^2$	$0.54m^2$
Airframe	No	Yes

Table 1 – Aircrafts' characteristic for ASWING's LLT validation

	NASA-GAW2		NACA4309
Re	9E5	1.4E6	2.65E5
cl_{alpha}	6.20	6.20	6.11
CL_{max}	1.5	1.7	1.2
CL_{min}	-0.5	-0.7	-0.3
$\alpha_{L=0}$	-4.25	-4.25	-3.9
cd_f	0.006	0.006	0.006
cd_p	0.002	0.002	0.0140

Table 2 – Airfoil 2D approximated data

as mentioned in [1]. The second aircraft under study is the configuration in [3] where CFD data are available for the case with and without the airframe/fuselage. Both configuration properties are sum up in tab 1. Xfoil analyses have been performed and the 2D approximated coefficients are recalled in Tab 2.

At the light of figures 5 and 7 one can witness that ASWING LLT predicts reasonably well the lift coefficient CL for a quite large range of angles of attack and can in the case of the second aircraft (as data were available) predict CL even for pre- and early stall. However, it won't predict post-stall CL as the implemented stall model does not recover the hysteresis stall phenomenon. Even though the fuselage has been implemented the effect on the lift is not captured especially at a higher angles of attack. The fuselage must have an impact on the surrounding flow that makes the wing stall earlier, such an impact is not captured by the volume influence function and slender body theory. One would notice that the variation of the fuselage section was not known. From [3] the airframe seems to face highly discontinuities in its sections which is not accurate with the slender body theory assumption. Thus one should expect better prediction of the near stall for the smoother fuselage.
Regarding Drag, the figure 6 shows the ASWING LLT CD prediction, note that it is quite accurate for a reasonable angle of attack. As the viscous contribution is taken into account in the drag computation, ASWING LLT can predict CD coefficient and consequently the CL/CD ratio making it an interesting tool for pre-design of rectangular tandem wings aircraft.

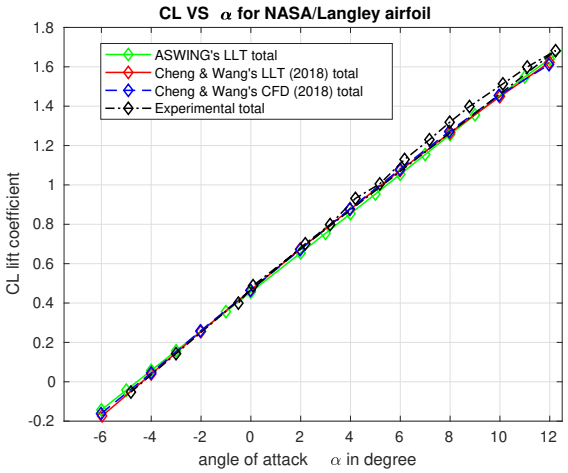

Figure 5 – Aircraft 1 : CL VS α predictions vs experimental data

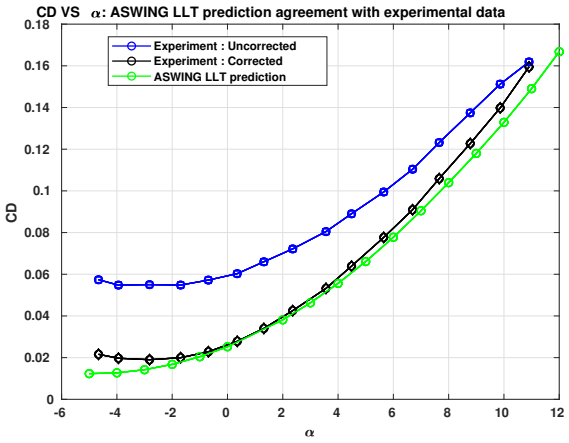

Figure 6 – Aircraft 1 : CD VS α agreement between Aswing's LLT and corrected experimental data

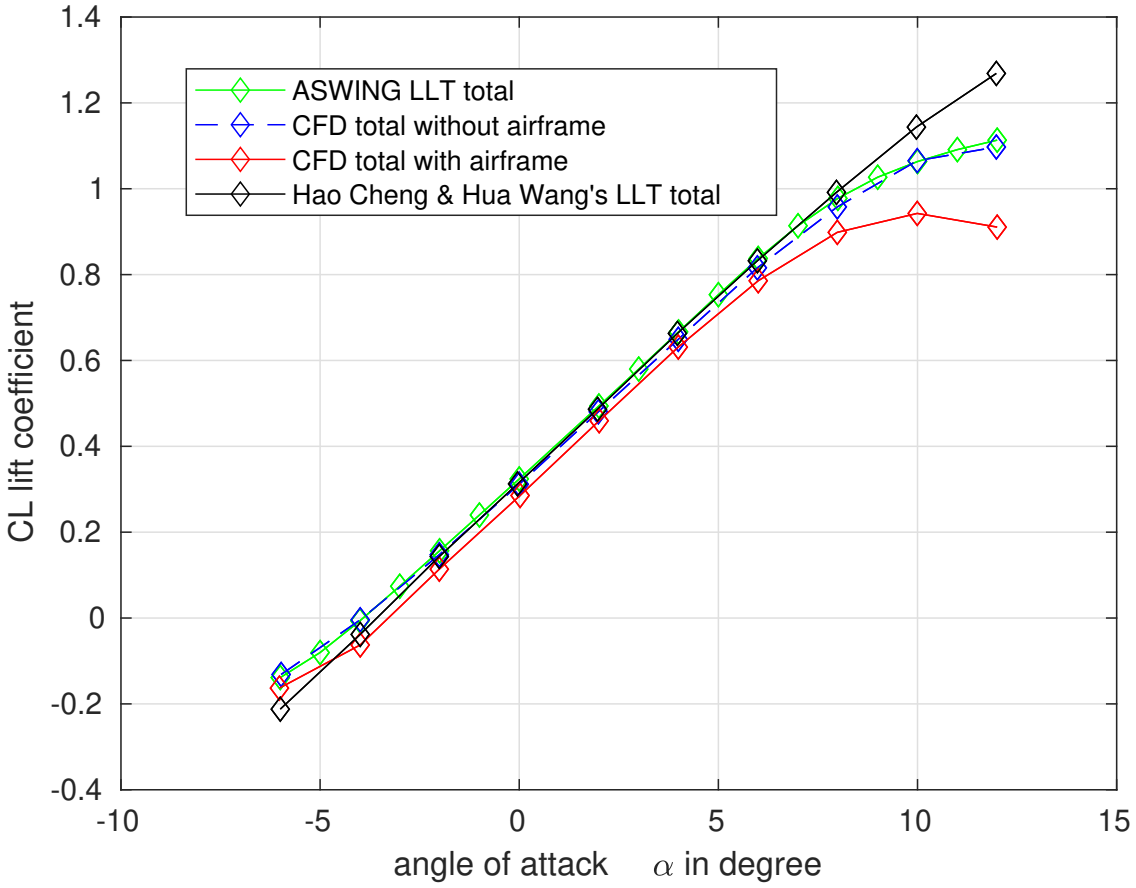

Figure 7 – Aircraft 2 : CL VS α, agreement between ASWING'LLT and CFD result for 2 cases : with and without the airframe on Cheng and Wang's tandem aircraft

4. Predicting lift and drag coefficient of quasi-eliptical/eliptical wing

The problem raised by elliptical wing is that the Reynold number varies elliptically along the span as it is a function of the local chord :

$$Re(y) = \frac{V_\infty}{\nu} c_0 \sqrt{1 - \left(\frac{2y}{b}\right)^2} \tag{32}$$

where c_0 and b are the root chord and span of the wing. Consequently the 2D airfoil properties (specially : cd_f, cd_p, cl_{max}, cl_{min} and α_0 varies along the span. Despite the Reynolds number varies elliptically, the airfoil properties do not. One should expect a different behaviour from a rectangular wing, in most of the cases cd_f, cd_p, cl_{min} are rising, cl_{max} decreases with the span. Thus taking the airfoil properties at the root chord would lead to an overestimated performance of the wing especially on drag and stall prediction.
To assess that problem, one must implement a spanwise-varying airfoil properties. Of course, one won't compute each coefficient for each chord discretized by the cosine method because it would be too time demanding. However, using a set of values and a bilinear interpolation would be efficient enough.

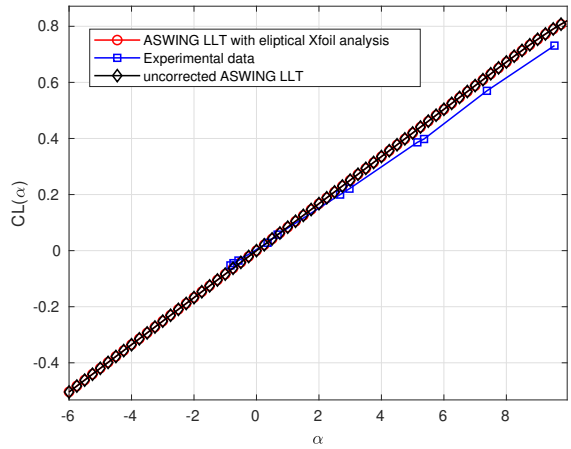

Figure 8 – $CL(\alpha)$ comparison with experimental data for eliptical wing

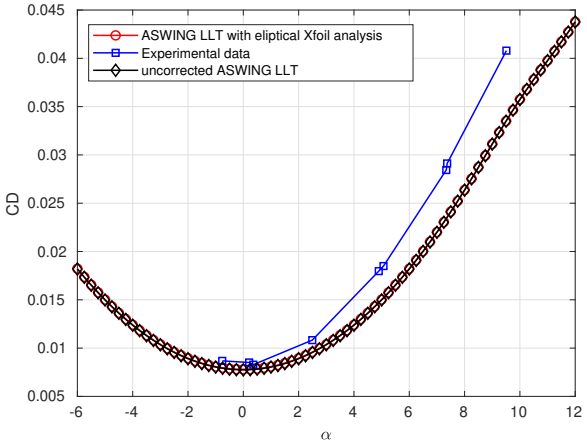

Figure 9 – $CD(\alpha)$ comparison with experimental data for eliptical wing

A comparison with experimental data from NASA Langley wind tunnel campaign [13] is proposed on figure 8 and 9. The wing under study is elliptical with a sifted leading edge so that the quarter chord line remains always perpendicular. The span and root chord are 1,83m and 0,33m for an aspect ratio of 7.7. The airfoil used to craft the wing is a NACA0012, the wing is under a flow with a velocity of 60m/s at sea-level atmospheric pressure. Note that the aspect ratio of the wing is quite low, which is a stress case for the lifting line theory.
Two numerical simulations have been fulfilled, the first one considers constant 2D airfoil properties from an XFOIL [12] analysis ran on the root chord. The second considers the variation of Reynolds number, when the chord value faces a 5% change from the previous one, a new XFOIL analysis is run. Both simulations use a cosine clustering method with 80 nodes.

The figure 8 and 9 present the CL and CD predictions of the numerical method versus the experimental data. One can note that CL is well predicted for a moderate angle of attack and becomes weaker for a high angle of attack. Regarding CD prediction, one can come to the same conclusion. The difference between the two numerical methods is almost imperceptible. The difference is around 1-2% better for the elliptical XFOIL analysis. This slight change is explained by figure 11, the viscous drag increase drastically after 80 percent of the span. However the chord is also varying concequently the local viscous drag does not increase that much as illustrated. Nevertheless one will prefer the more precise method despite this extra calculus's cost.

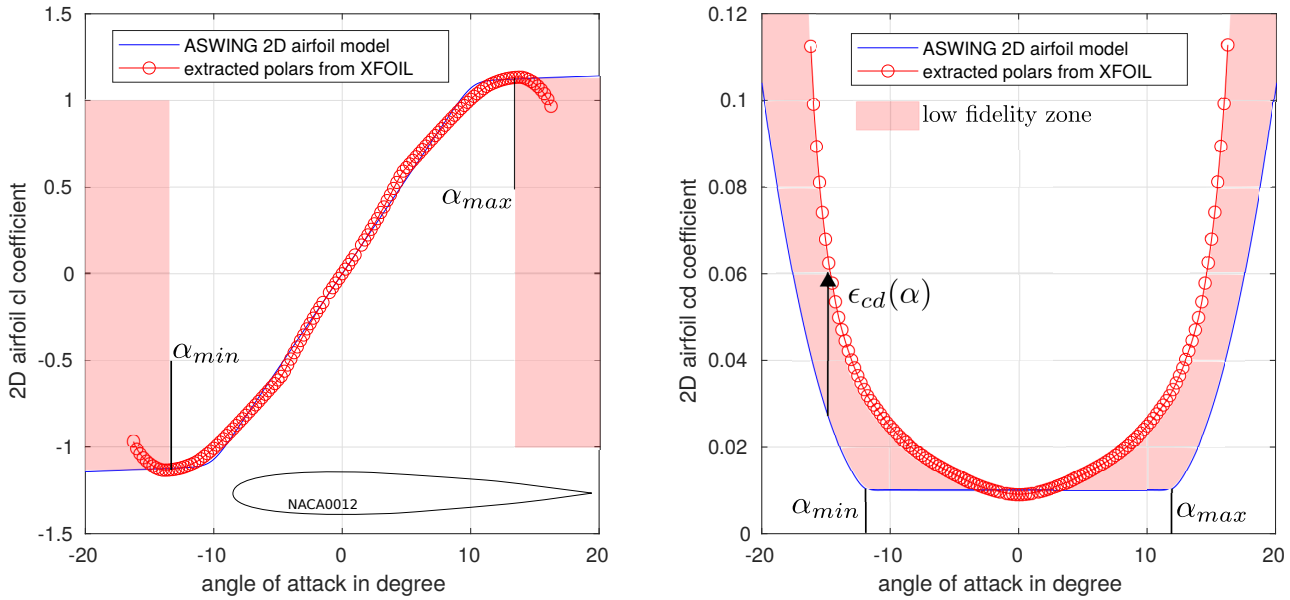

Figure 10 – airfoil cl and cd approximation under ASWING vs XFOIL analysis for a NACA0012 at Re = 200 000

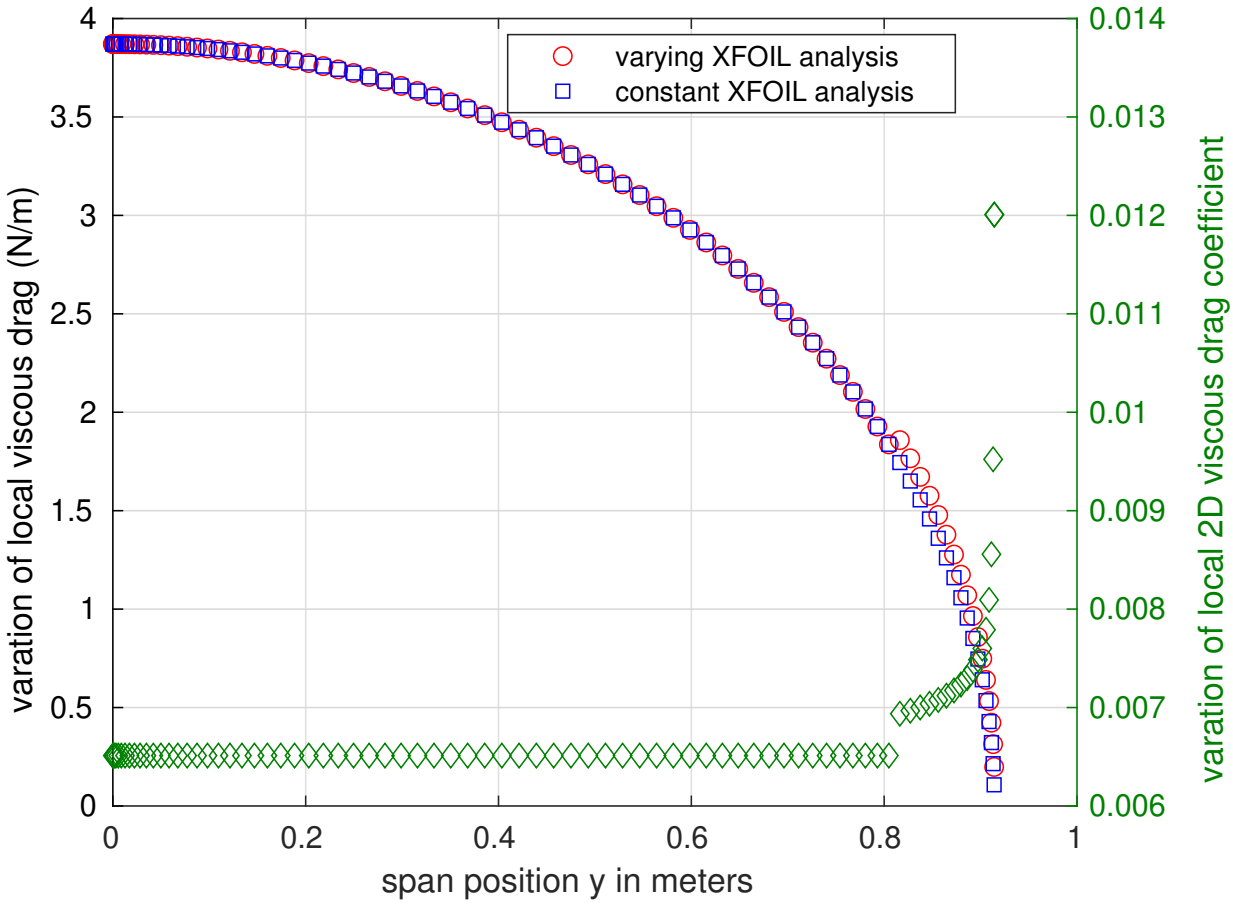

Figure 11 – Comparison of viscous drag between the chord varying and the constant XFOIL analysis

Regarding the divergence of drag prediction for high angle of attack in both case (rectangular and eliptical planforms), this error is mainly due to the drag approximation model illustrated on figure 10. Indeed the local cd error increases with angle of attack. A improvement could be to implement a func-

	Mowe initial	Mowe final
Airfoil	NACA4309	NACA4309
Speed	V = 30.0m/s	V = 30m/s
Re	4.2E5 (root)	4.2E5 (root)
Planform	Q-Eliptical (0.42)	Q-Eliptical (0.42)
efficiency	0.9892	0.9892
c_1	0.21m (root)	0.21m (root)
c_2	0.21m (root)	0.21m (root)
b_1	2.55m	2.55m
b_2	2.55m	2.55m
ϑ_1	2 degrees	2 degrees
ϑ_2	2 degrees	2 degrees
Λ_1	0	+5 degrees
Λ_2	0	-5 degrees
G (gap)	0.0m	-0.5c_1
S (Stagger)	3.0c_1	3.0c_1
S_{ref}	$9.31E-01m^2$	$9.31E-01m^2$
Airframe	R = 0.5c_1	R = 0.5c_1

Table 3 – Tandem aircraft with quasi-eliptical wing planform before and after optimization

tion under ASWING that interrogates the polars depending on the local angle of attack and Reynolds number, which is out of this article's scope.
As it can be see on the figure 9 and 8 even in the most demanding case, the ASWING steady aerodynamic model remains quite precise and represents an interesting tool for pre-design of high aspect ratio tandem aircraft with elliptical planform. Note that in the next section one will only study planform with a minimum aspect ratio of 10 to avoid any errors on lift and drag prediction due to LLT limitations.

5. Parametric Study of tandem aircraft with high aspect ratio quasi eliptical planform

5.1 Stagger impact:

The distance between the wings can have a positive impact on CL over CD ratio as shown by [3] . However, the main problem in the study is that they did not take into account the fuselage's drag. In that case one has performed an analysis with stagger varying from 2.5c_1 to 6.5c_1. Figure 12 shows that one recovers the same conclusion for positive effect for the case with no frame. However when one takes into account the fuselage drag the tendency is opposite meaning that the positive impact of stagger on wing interactions is less important than the induced drag generated by the fuselage.

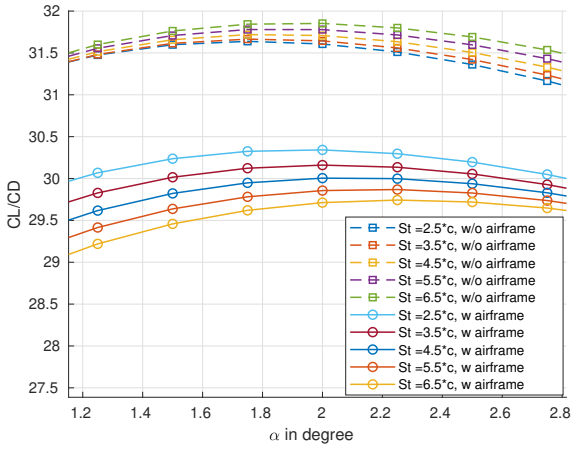

Figure 12 – Stagger effect on CL/CD ratio with and without airframe

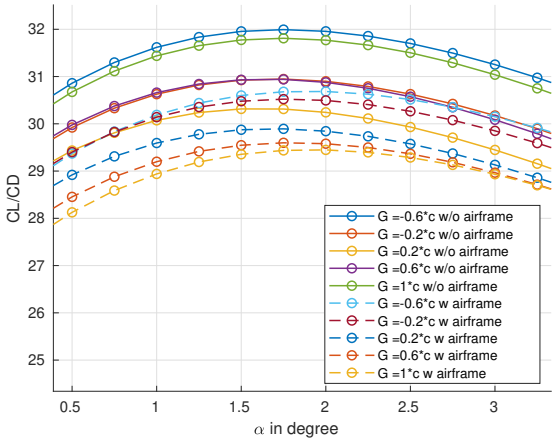

Figure 13 – Gap effect on CL/CD ratio with and without airframe

5.2 Gap effect:

As well as the stagger, the gap has a direct impact on fuselage thickness as it is the physical connection between the wings. In the simulation, the gap is varying from 0.5c to 1.0c. From figure 13, one can witness that the tendency does not invert by taking into account the fuselage or not, meaning that a negative gap has still a better impact than a positive one no matter there is a fuselage or not. Note that it is still more accurate to take into account the fuselage impact as it will less overestimate the CL/CD ratio.

5.3 Twist effect:

ϑ_1 and ϑ_2 have been studied to see their effect on the maximum CL/CD ratio. Simulations have been performed firstly with ϑ_1 varying with ϑ_2 constant and secondly reversed. From figures 14 and 15 one can witness that the main effect of twist angle is to shift the maximum CL/CD ratio angle of attack. Nevertheless, one can notify as well a positive impact of negative ϑ_1. Indeed when the wing is negatively twisted, its trailing edges are rotated upward decreasing slightly the impact of the trailing vortices of the front wing on the backward one. One can not recover however the same conclusion for the effect of a twist angle on the backward wing.

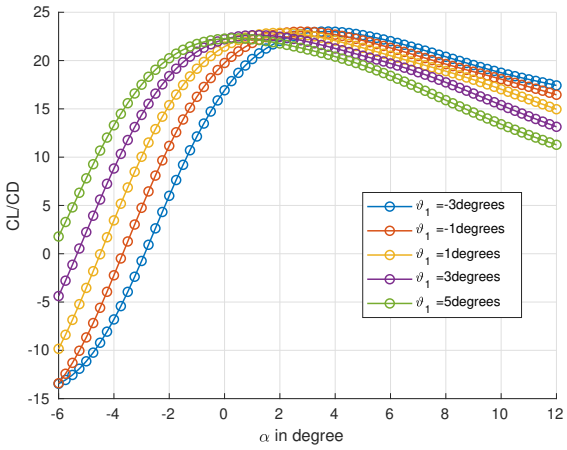

Figure 14 – ϑ_1 effect on CL over CD ratio

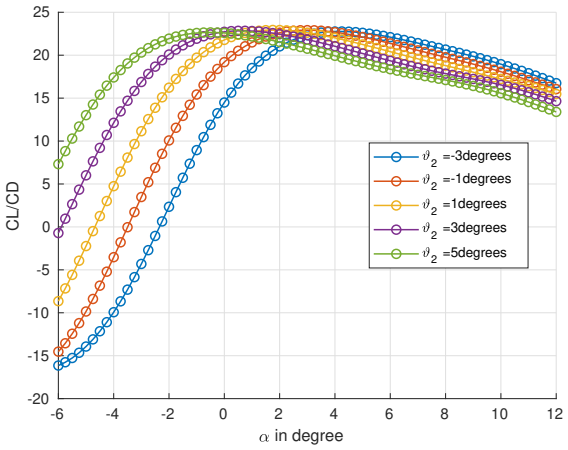

Figure 15 – ϑ_2 effect on CL over CD ratio

5.4 Dihedral effect:

The last parametric study regards the dihedral angle of each wing. Four simulations have been performed, the first one is a positive varying Λ_1 angle for a constant Λ_2, the second is a positive varying Λ_2 angle for constant Λ_1, the third is a dual positive equal varying Λ_1 and Λ_2 and finally an inverted Λ_1 and Λ_2.

According to Figure 16 a positive Λ_1 dihedral angle has a positive impact on CL/CD ratio, indeed as the geometry of the front wing rotated upward, the trailing vortices have less impact on the backward wing.
Logically in the light of Figure 17, a positive Λ_2 dihedral angle has a negative impact as the geometry is more aligned with the trailing vortices of the front wing.
A positive equal dihedral angle seems to not increase the CL/CD ratio as described by Figure 18
Finally, a dual inverted dihedral angle seems to represent the most positive situation according to Figure 19. In fact, the trailing vortices plans become more and more independent thanks to this kind of geometry reducing the impact of the front wing on the backward wing.

5.5 Final Geometry:

In the light of the previous parametric study, one converges to an optimal geometry that tends to maximise the CL/CD ratio. The final and initial geometry is summed up in 3. Note that in comparison

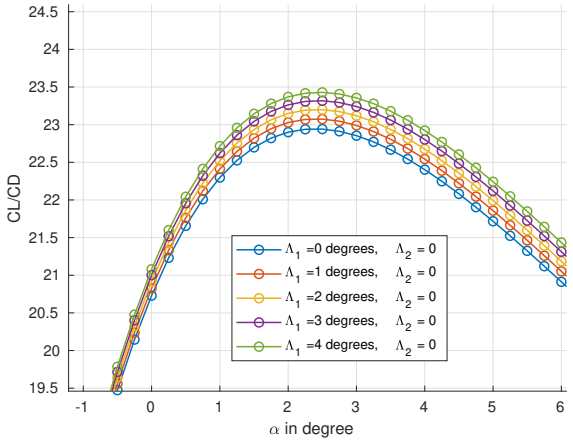

Figure 16 – Λ_1 effect on CL over CD ratio

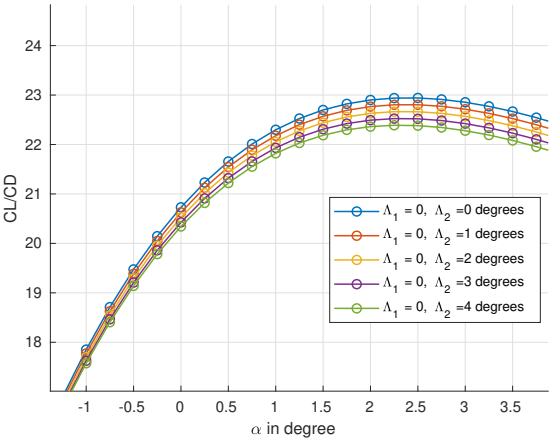

Figure 17 – Λ_2 effect on CL over CD ratio

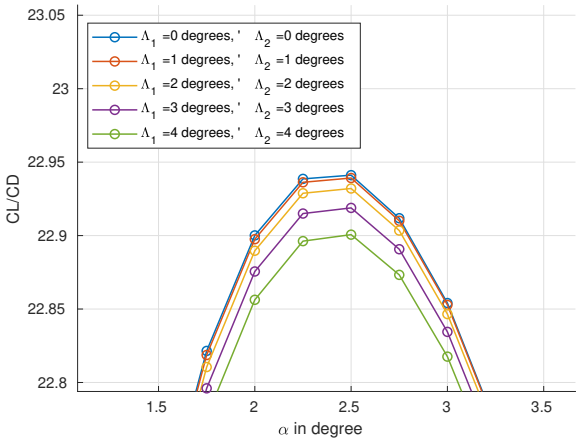

Figure 18 – $\Lambda_1 + \Lambda_2$ same orientation effect on CL over CD ratio

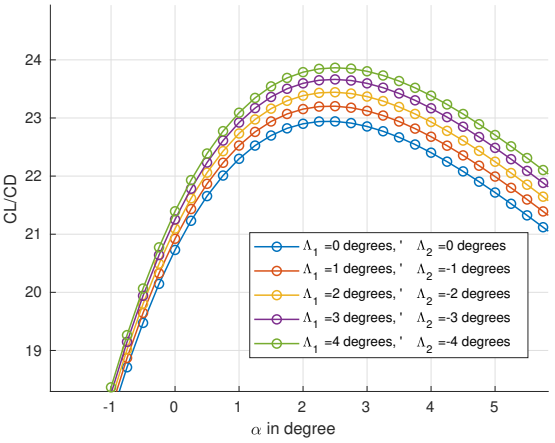

Figure 19 – $\Lambda_1 + \Lambda_2$ inverted orientation effect on CL over CD ratio

to the initial geometry one has an improvement of 9.6% of the CL/CD ratio as recalled by the Figure 21

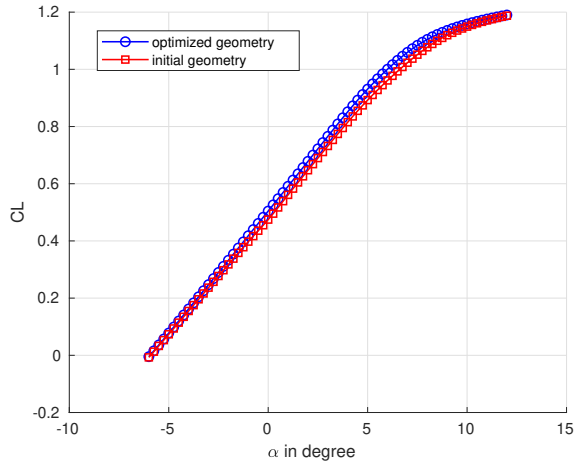

Figure 20 – CL(α) comprison between baseline and optimized geometry

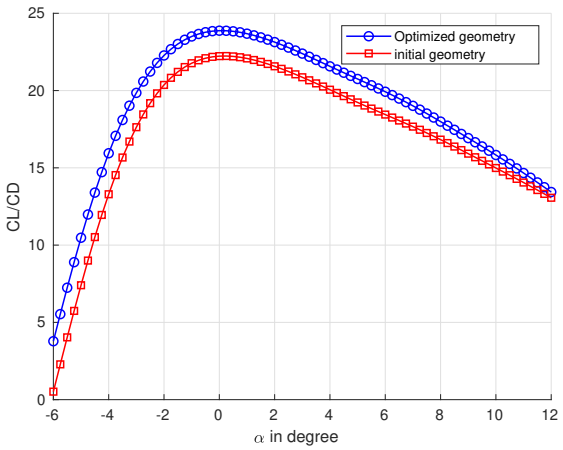

Figure 21 – $\frac{CL}{CD}(\alpha)$ for final VS initial geometry

6. Conclusion:

As shown in the previous sections, ASWING can predict the lift coefficient of tandem aircraft with both rectangular or elliptical planform up to pre stall angles of attack. Care must be taken on the shape of the aircraft's fuselage understudy to fit with slender body theory assumptions. In that case, ASWING will predict non overestimated performance as it take into account the fuselage's induced drag.

A modified airfoil XFOIL analysis has been proposed to have better accuracy for drag prediction for chord varying planform.

ASWING can predict total and induced drag for reasonable angles of attack making it a good pre-design performance prediction tool.

Finally, an extended application case has been presented based on the [3] study to maximize the CL/CD ratio of a tandem aircraft studying the effect of twist, dihedral, stagger gap and fuselage impact. The study has shown that significant improvement can be obtained by choosing the right parameters.

However, the proposed optimized geometry must also be studied regarding flight stability which can be performed also under ASWING.

7. Contact Author Email Address

Romain JAN : romain.jan@isae-supaero.fr
Prof Jean-Marc Moschetta : jean-marc.moschetta@isae-supaero.fr
Prof Jean-Philippe Condomines : jean-philippe.condomines@enac.fr

8. Copyright Statement

References

[1] T. W. Feistel, V. R. Corsiglia, and D. B. Levin, "Wind-Tunnel Measurements of Wing-Canard Interference and a Comparison with Various Theories," Feb. 1981.

[2] E. V. Laitone, "Prandtl's biplane theory applied to canard and tandem aircraft," *Journal of Aircraft*, vol. 17, pp. 233–237, Apr. 1980.

[3] H. Cheng and H. Wang, "Prediction of Lift Coefficient for Tandem Wing Configuration or Multiple-Lifting-Surface System Using Prandtl's Lifting-Line Theory," *International Journal of Aerospace Engineering*, vol. 2018, pp. 1–15, July 2018.

[4] G. Q. Zhang and S. C. M. Yu, "Unsteady Aerodynamics of a Morphing Tandem-Wing Unmanned Aerial Vehicle," *Journal of Aircraft*, vol. 49, pp. 1315–1323, Sept. 2012.

[5] M. D. Rhodes and B. P. Selberg, "Benefits of dual wings over single wings for high-performance business airplanes," *Journal of Aircraft*, vol. 21, pp. 116–127, Feb. 1984.

[6] "Aerodynamic design and control of tandem wing unmanned aerial vehicle, master thesis, middle east technical university, 2019,"

[7] D. F. Scharpf and T. J. Mueller, "Experimental study of a low Reynolds number tandem airfoil configuration," *Journal of Aircraft*, vol. 29, pp. 231–236, Mar. 1992.

[8] M. R. Ahmed and Y. Kohama, "Experimental Investigation on the Aerodynamic Characteristics of a Tandem Wing Configuration in Close Ground Proximity.," *JSME International Journal Series B*, vol. 42, no. 4, pp. 612–618, 1999.

[9] T. M. Broering and Y.-S. Lian, "The effect of phase angle and wing spacing on tandem flapping wings," *Acta Mechanica Sinica*, vol. 28, pp. 1557–1571, Dec. 2012.

[10] M. Drela, "ASWING 5.86 Technical Description — Steady Formulation," p. 57.

[11] M. Drela, "Integrated simulation model for preliminary aerodynamic, structural, and control-law design of aircraft," in *40th Structures, Structural Dynamics, and Materials Conference and Exhibit*, (St. Louis,MO,U.S.A.), American Institute of Aeronautics and Astronautics, Apr. 1999.

[12] M. Drela, "XFOIL: An Analysis and Design System for Low Reynolds Number Airfoils," in *Low Reynolds Number Aerodynamics* (C. A. Brebbia, S. A. Orszag, J. H. Seinfeld, P. Spanos, A. S. Cakmak, P. Silvester, C. S. Desai, G. Pinder, R. McCrory, S. Yip, F. A. Leckie, A. R. S. Ponter, K.-P. Holz, K.-J. Bathe, J. Connor, W. Wunderlich, J. Argyris, and T. J. Mueller, eds.), vol. 54, pp. 1–12, Berlin, Heidelberg: Springer Berlin Heidelberg, 1989. Series Title: Lecture Notes in Engineering.

[13] Raymond E Mineck and Paul M H W Wijgen, "Wind-Tunnel Investigation of Aerodynamic Efficiency of three Planar Elliptical Wings With curvature of quarter-chord line," *NASA Technical Paper*, 1993.